Microstructural influence of the thermal behavior of arc deposited TiAlN coatings with high aluminum content

Journal of Alloys and Compounds 854 (2021) 157205

Contents lists available at ScienceDirect

Journal of Alloys and Compounds

journal homepage: http://www.elsevier.com/locate/jalcom

Microstructural influence of the thermal behavior of arc deposited TiAlN coatings with high aluminum content

A.B.B. Chaar [a, b], L. Rogström [a], M.P. Johansson-Jöesaar [a, c], J. Barrirero [a, b], H. Aboulfadl [b, d], N. Schell [e], D. Ostach [e], F. Mücklich [b], M. Odén [a, *]

[a] Nanostructured Materials, Department of Physics, Chemistry and Biology, Linköping University, SE-58183, Linköping, Sweden
[b] Department of Materials Science, Saarland University, D-66123, Saarbrücken, Germany
[c] Seco Tools AB, SE-737 82, Fagersta, Sweden
[d] Department of Physics, Chalmers University of Technology, SE-41296, Göteborg, Sweden
[e] Institute of Materials Research, Helmholtz Zentrum Geesthacht, D-21502, Geesthacht, Germany

ARTICLE INFO

Article history:
Received 5 July 2020
Received in revised form
25 August 2020
Accepted 14 September 2020
Available online 17 September 2020

Keywords:
Coating materials
Microstructure
Vapor deposition
Synchrotron radiation

ABSTRACT

The influence of the microstructure on the thermal behavior of cathodic arc deposited TiAlN coatings was studied as a function of isothermal annealing. Two compositionally similar but structurally different coatings were compared, a $Ti_{0.34}Al_{0.66}N_{0.96}$ coating with a fine-grain structure consisting of a mixture of cubic (c) and hexagonal (h) phases, and a $Ti_{0.40}Al_{0.60}N_{0.94}$ coating with a coarse-grain structure of cubic phase. By *in situ* wide-angle synchrotron x-ray scattering, spinodal decomposition was confirmed in both coatings. The increased amount of internal interfaces lowered the decomposition temperature by 50 °C for the dual-phase coating. During the subsequent isothermal anneal at 1000 °C, a transformation from c-AlN to h-AlN took place in both coatings. After 50 min of isothermal annealing, atom probe tomography detected small amounts of Al (~2 at.%) in the c-TiN rich domains and small amounts of Ti (~1 at.%) in the h-AlN rich domains of the coarse-grained single-phase $Ti_{0.40}Al_{0.60}N_{0.94}$ coating. Similarly, at the same conditions, the fine-grained dual-phase $Ti_{0.34}Al_{0.66}N_{0.96}$ coating exhibits a higher Al content (~5 at.%) in the c-TiN rich domains and higher Ti content (~15 at.%) in the h-AlN rich domains. The study shows that the thermal stability of TiAlN is affected by the microstructure and that it can be used to tune the reaction pathway of decomposition favorably.

1. Introduction

TiAlN-alloys are frequently used as protective thin coatings, example metal in cutting tools, because of their advantageous high temperature properties [1]. At elevated temperatures c-TiAlN exhibits spinodal decomposition, resulting in coherent nm-sized domains that are rich in c-TiN or c-AlN [2]. The associated coherency strains between these phases, in combination with their differences in elastic properties, effectively inhibit dislocation movements resulting in age hardening and improved mechanical properties [3,4]. The subsequent phase transformation of c-AlN to h-AlN renders formation of incoherent grain boundaries [5,6] that deteriorates the mechanical properties of TiAlN coatings [7].

The effect of varying the chemical composition both in terms of the metal ratio (Ti/Al) [8,9] and nitrogen [10–12] on the high temperature transformation of $(Ti_{1-x}Al_x)N_y$ have been extensively studied. Such studies have resulted in different types of phase diagrams of metastable phases that may form [13,14].

The cubic phase is stabilized by temperature or pressure at approximately 3200 K or 12 GPa [15]. Such extreme conditions normally do not prevail in applications where TiAlN is used, e.g. metal cutting operations. Instead stabilization is improved by growing multilayers or by adding different alloying elements [16–19]. Both multilayering and alloying alter the decomposition pathway of the cubic phase [20,21]. Stabilization of the cubic phase has also triggered the development of a hybrid magnetron sputtering/HiPIMS deposition technique where the ion energy of Ti and Al can be tuned independently such that a wider compositional range than normal can be deposited [22,23]. Common to all these studies is that the as-deposited microstructure obtained depends on the deposition technique and deposition conditions used, as discussed by Andersson et al. [24] and Hans et al. [25]. However, the

* Corresponding author.
E-mail address: magnus.oden@liu.se (M. Odén).

https://doi.org/10.1016/j.jallcom.2020.157205

impact of the different microstructures obtained on the high temperature decomposition pathway is less explored. Perhaps one reason for the lack of such studies is the difficulty associated with isolating the effect of microstructure from the effects of chemical composition.

The decomposition pathway of one microstructure was investigated in detail by Rachbauer et al. [26] where they point out the influence of microstrain on the reaction kinetics. The importance of strain on the reaction kinetics was further discussed by Rogström et al. [27] where they used a combination of *in situ* high temperature strain measurements and phase field modelling to characterize the spinodal decomposition process. The microstrain is closely related to the microstructure and the different defects generated during coating growth. The strain concentrations at such defects may also affect the high temperature behavior of the coating [28]. The influence of the microstructure is also stressed in the work by Rafaja et al. [29] and Norrby et al. [6] concerning transformations from the cubic to the hexagonal phase in TiAlN.

Recently, we reported a growth-related study on the possibility to alter the arc plasma properties by applying an additional magnetic field perpendicular to the cathode surface [30]. By increasing the magnetic field strength, the plasma plume is expanded and the plasma density decreased. Additionally, it reduces the available electrons in front of the cathode and thereby lowers the probability of electron-collisional events especially related to ionization of N_2. With this deposition setup, it is possible to grow coatings with different microstructures without significantly changing their chemical composition.

In this study, we have taken advantage of this possibility and grown two distinctly different microstructures, i.e. one fine-grained dual-phase coating and one coarse-grained single-phase coating with similar compositions. These coatings are then subjected to high temperature anneals and their different decomposition pathways are determined. We used *in situ* synchrotron wide-angle x-ray scattering to follow their decomposition process at 1000 °C. This was supplemented by atom probe tomography (APT) to determine the local chemical composition in combination with transmission electron microscopy.

2. Experimental details

TiAlN coatings were deposited in an industrial scale arc deposition system (Oerlikon Balzers Innova, Balzers, Liechtenstein) designed to coat thousands of cutting tool inserts in each batch. Arc sources were positioned on the chamber wall, facing the center of the deposition system and thus also the sample fixture. Three sources were placed 120° apart and at the same height to cover the upper half of the sample fixture. The remaining three sources were similarly placed but at a lower level in the chamber to cover the lower half of the fixture. For the current study, $Ti_{0.33}Al_{0.67}$ composite cathodes, 160 mm in diameter and 15 mm thick, were mounted on all arc sources. The selected magnetic assembly system, for each arc source, consisted of permanent magnets and a supplementary electromagnetic coil. Fig. 1 shows a schematic of the arc source configuration, consisting of a combination of an electromagnetic coil and permanent magnets located at the cathode backside, and a ring-shaped anode positioned around the cathode.

TiAlN coatings were grown on cemented carbide WC-12 wt% Co inserts (ISO SNUN120408) and 10 cm × 10 cm × 0.25 μm thick iron foils (FE00040, Goodfellow Cambridge Ltd, Huntingdon, UK). Prior to depositions, the substrates were ultrasonically cleaned in an alkali solution followed by alcohol, after which they were vertically positioned on a one-fold rotating fixture. The deposition system was evacuated to a pressure of less than 2.0×10^{-3} Pa, and then the substrates were Ar-etched for about 30 min at 0.2 Pa with a direct

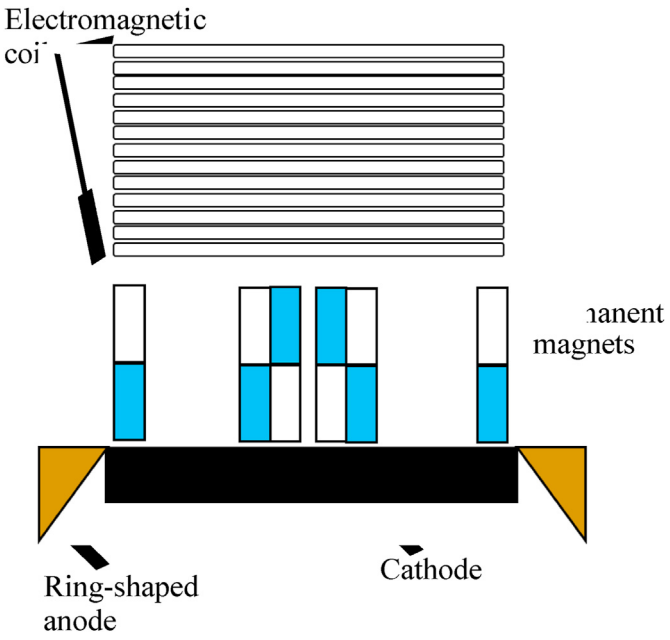

Fig. 1. Top-view schematic of the arc source (not to scale).

current bias voltage of −170 V. The TiAlN coatings were grown in a reactive 3.5 Pa N_2 atmosphere, a cathode current of 180 A, a process temperature of 480 °C, negative substrate bias voltage of 60 V, and coil currents of 0 and 2 A, applied individually in distinct deposition runs. It resulted in two coatings, which are labelled dual-phase and single-phase coatings based on previous experiments [36]. The resulting coating thicknesses are 15 and 9 μm (see Table 2), corresponding to deposition rates of 120 and 60 nm/min, respectively. Powder samples were obtained from the as-deposited TiAlN coatings by dissolving the coated Fe foils in hydrochloric acid 37%. The coating powder was then collected, cleaned with deionized water and acetone, and mortared to a fine powder.

The coating thickness was evaluated from fractured insert cross sections in a Leo 1550 Gemini Scanning Electron Microscope (SEM) (Zeiss, Oberkochen, Germany) with a work distance of 5 mm and an acceleration voltage of 5 kV.

The coating structure was investigated by transmission electron microscopy (TEM) in a FEI Tecnai G° TF20 UT Analytical (ThermoFisher Scientific, Hillsboro, OR, USA) operated with an accelerating voltage of 200 kV. Cross sectional segments of TiAlN on substrates were cut and mechanical polished according to the procedure in Refs. [31]. To achieve electron transparency, a final polishing was performed in a Gatan Precision Ion Polishing System (PIPS) (Gatan, Pleasanton, CA, USA) with energies varying from 5 keV to 1 keV. TEM images were analyzed with Gatan DigitalMicrographTM software (version 3.4). Diffraction pattern simulation were performed with the JEMS Electron Microscope software (version 3.7624U2012) and used as comparison to the obtained Fast-Fourier transformation (FFT) diffraction pattern.

Wide-angle x-ray scattering (WAXS) was performed at beamline P07, Petra III of the German Electron Synchrotron facilities (DESY) in Hamburg, Germany. The *in situ* measurements were performed during isothermal annealing at 1000 °C for 3 h in a vacuum chamber at a pressure less than 1.2×10^{-3} Pa. The heating and cooling rates were 20 °C/min. Two separate experiments were performed to investigate the phase and microstructure evolution and the strain evolution, respectively. The diffracted intensity was recorded with a 2D PerkinElmer detector positioned behind the sample (see Fig. 2) and the sample-to-detector distance was

determined by a NIST LaB_6 standard sample. Table 1 shows the details of both experiments. To study the phase and microstructure evolution, powder samples were placed on an alumina holder, and the x-ray beam was transmitted through the sample. The two-dimensional exposures were transformed into one-dimensional lineouts by integration in 20° wide azimuthal bins (Ψ). The FWHM and plane spacing were extracted by fitting pseudo-Voigt functions to the one-dimensional lineouts, and the average values for all azimuthal bins were calculated. To study the strain evolution, 1 mm thick slices of coated WC-Co substrates were used, and the x-ray beam was transmitted through the coating. The data was integrated in 10° wide azimuthal bins, and pseudo-Voigt functions were fitted to the peaks to extract the peak position. The strain in the in-plane direction was determined by the $\sin^2\psi$ method [32].

The global and local compositions of TiAlN powder, in the as-deposited state and post-annealed at 1000 °C for 50 min, were analyzed by Laser Pulsed Atom Probe Tomography with a CAMECA LEAP™ 3000X HR instrument (CAMECA, Madison, WI, USA). A repetition rate of 100 kHz and a specimen temperature of about −213 °C were used. The pressure was lower than 1×10^{-10} Torr (1.33×10^{-8} Pa), and the laser pulse energy was set to 0.7 nJ. The evaporation rate was 5 atoms per 1000 pulses. Datasets were reconstructed with the CAMECA IVAS™ 3.6.8 software. APT sample preparation was carried out with a dual-beam FEI Helios NanoLab 600™ Focused Ion Beam (ThermoFisher Scientific, Hillsboro, OR, USA) in a Scanning Electron Microscopy workstation (FIB/SEM) by the lift-out technique [33]. A 250 nm thick Pt-cap layer was first deposited to protect the material from gallium implantation. After thinning of the specimens to a needle-like shape, a low energy milling at 2 kV was performed to minimize the Ga induced damage. The atomic distribution randomness in the as-deposited samples was evaluated by a frequency distribution analysis (FDA). In FDA, the actual distribution of atoms is compared to a completely random dataset described by a binomial probability distribution [34]. A chi-square significance test with a significance value of $p < 0.05$ was chosen to reject the null hypothesis and indicate whether there is a deviation from randomness in the arrangements of atoms through the dataset. Samples deviating from randomness were analyzed by two-dimensional concentration and density maps, and proximity histograms were constructed from iso-concentration and iso-density surfaces [35,36].

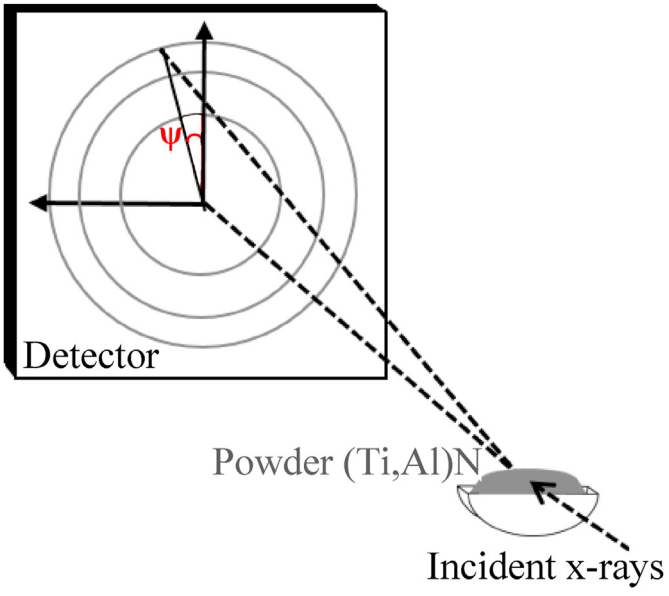

Fig. 2. Schematic setup of the *in situ* synchrotron WAXS experiment.

The coating hardness (H) was recorded with an UMIS 2000 nanoindenter (Fischer-Cripps, Sydney, Australia) equipped with a Berkovich diamond tip using a maximum load of 50 mN. The tip area function was determined by indents in a fused-silica reference. At least 30 indentations were used to extract the average hardness of the coatings using the Oliver-Pharr method [37]. Measurements were performed on tapered cross sections, polished to a mirror-like finish to minimize the influence of roughness.

3. Results and discussion

We start by describing the two coatings with different microstructures used in this study. Then we report and discuss their different decomposition pathways at elevated temperature. Finally, we address the influence of the different decomposition pathways on mechanical properties.

The thickness measured by SEM and the global composition determined by APT of the investigated TiAlN coatings in the as-deposited state are given in Table 2. The composition of the single-phase coating has a slightly lower Al-content compared to the dual-phase coating, which is caused by slightly different directional distribution of Al and Ti ions when emitted from the cathode spot [30]. The wider directional distributions and the higher resputtering rate of Al compared to Ti [38] results in a slightly lower atomic metal ratio ([Al]/[Ti]) in the coatings compared to the cathode. Both coatings are found to be somewhat under-stoichiometric with respect to nitrogen. The nitrogen content of the single-phase coating is slightly lower than the dual-phase coating, which is consistent with previous observation of TiAlN coatings grown at similar N_2 partial pressures [39]. Due to the high number of multiple events on the detector when measuring nitrides with APT, a slight underestimation of nitrogen of 1–2 at.% cannot be excluded [40,41].

Fig. 3(a) shows a bright-field TEM micrograph of the as-deposited dual-phase $Ti_{0.34}Al_{0.66}N_{0.96}$ coating, revealing a columnar structure with large domains (bright contrast) and nanometric domains (dark contrast) The selected area electron diffraction (SAED) pattern in Fig. 3(b) confirms the presence of both cubic and hexagonal phases. Fig. 3(e) shows a high-resolution micrograph (HRTEM) of the same sample, and the corresponding FFT in Fig. 3(c) displays a pattern of slightly misoriented hexagonal and cubic domains. Fig. 3(d) shows a diffraction pattern that has been generated with the software Java Electron Microscope Simulation (JEMS) and was used to identify the hexagonal phase. The hexagonal $10\bar{1}0$ spots were selected to construct an inverse-FFT image (Fig. 3(f)). The bright areas reveal fine h-AlN domains elongated in the growth direction. Similar to what has previously been observed for Mode I grown coatings, this is a result of growth subjected to a higher degree of ionization and, consequently, a higher charge-to-mass arrival ratio and a higher energy flux to the coating growth front, which is sufficient for nucleation of h-AlN in addition to c-TiAlN [30]. Simultaneous nucleations of the cubic and hexagonal phases lead to competitive growth, resulting in a fine-grained structure. Fig. 3(g) shows the cubic single-phase $Ti_{0.40}Al_{0.60}N_{0.94}$ coating. It displays a dense microstructure consisting of coarse columns (100–200 nm wide). In this case, the applied magnetic field on the cathode surface (Mode II) results in a lower ionization of plasma species, and thus lower charge-to-mass ratio and energy delivered at the growth front compared to Mode I, which suppresses the nucleation of the hexagonal phase, and leads to the growth of single-phase c-TiAlN coatings [30].

The phase content of the as-deposited coating is thus in agreement with the “single-phase” and “dual-phase” labelling. It should, however, be noted that the sample labels are kept the same

Table 1
Details of the *in situ* wide-angle scattering experiments.

Experiment	Sample	X-ray energy (keV)	Beam size (μm^2)	Exposure time (s)	Sample-detector distance (mm)
Phase and microstructure	Coating powder	53.7	100 × 100	16	2954
Strain	Coated WC-Co	87.1	100 × 100	8	1947

Table 2
Cathode and APT global composition of powder coatings in the as-deposited state, and approximate coating thickness on WC-Co substrate.

Sample	Thickness (μm)	As-deposited composition (at.%)				
		Cathode	Ti	Al	N	Coating
Dual-phase	15	$Ti_{0.33}Al_{0.67}$	17.7 ± 0.1	34.2 ± 0.4	48.0 ± 0.4	$Ti_{0.34}Al_{0.66}N_{0.96}$
Single-phase	9		20.8 ± 0.6	31.8 ± 0.3	46.8 ± 0.6	$Ti_{0.40}Al_{0.60}N_{0.94}$

for the heat-treated samples and thus always indicate their as-deposited structure.

Prior to APT characterization (Figs. 4 and 8), specimens of as-deposited single-phase and dual-phase coatings were analyzed by frequency distribution analysis (FDA). All analyzed specimens of the single-phase sample showed a random (homogeneous) distribution, while only half of the analyzed specimens of the dual-phase samples showed homogeneous distribution. The second half of specimens from the dual-phase sample show inhomogeneous atom distribution, that is the presence of regions with different chemical composition from the rest of the specimen caused by local concentration of certain atoms. Inhomogeneous specimens of the dual-phase samples were further analyzed by two-dimensional concentration and density maps, and similar results were observed between the samples.

Fig. 4 shows the APT results, which consists of a 2D iso-concentration map (Fig. 4(a)) and a 2D iso-density map of the dual-phase $Ti_{0.34}Al_{0.66}N_{0.96}$ coating containing both cubic and hexagonal phases (Fig. 4(b)). The results show only a slight variation in the Al content over the sample volume, while an area of higher density exists in the lower right corner. Density heterogeneities in iso-density maps may occur due to different field evaporation potentials during the APT acquisition, often as a result of differences in crystal structure and their respective atomic bonding [42]. Since high-density regions were not observed in the single-phase cubic $Ti_{0.40}Al_{0.60}N_{0.94}$ coating, such regions have been attributed to hexagonal-structured domains and, consequently, the cubic phase is represented in the surrounding regions with lower density.

Fig. 4(c) shows a proximity histogram of the concentration profile through the hexagonal and cubic regions in Fig. 4(b), constructed by measuring the concentration average perpendicular to the boundary. Furthermore, as shown in the table inset in Fig. 4(c), the composition profiles of the hexagonal and cubic phase regions are very similar with only a small difference in the average Al concentration of approximately 2 at.%. This behavior suggests a limited adatom diffusivity during growth which hinders the formation of stoichiometric binary phases. Implantation of high-energy ions is correlated to an increased amount of intermixing, resulting in growth of cubic and hexagonal solid solution phases [30]. The formation of h-TiAlN solid solution phases has also been observed in other studies [43,44] and can be grown as epitaxial layers [45].

Fig. 5 shows WAXS lineouts from the as-deposited state (dashed lines) until the end of the 1000 °C-annealing. The as-deposited single-phase $Ti_{0.40}Al_{0.60}N_{0.94}$ coating (Fig. 5(b)) exhibits a solid solution cubic phase, while a cubic and hexagonal phase mixture is identified for the $Ti_{0.34}Al_{0.66}N_{0.96}$ coating (Fig. 5(a)), consistent with the TEM-observations. During the increase of annealing temperature up to 1000 °C, both phases spinodally decomposed into coherent cubic TiN-rich and AlN-rich domains, observed as broadening of the indexed c-TiAlN diffraction peaks. For the single-phase $Ti_{0.40}Al_{0.60}N_{0.94}$ coating, this is followed by the appearance of hexagonal phase diffraction peaks, indexed h-AlN, that sharpen during further isothermal annealing. The hexagonal diffraction peaks of the dual-phase $Ti_{0.34}Al_{0.66}N_{0.96}$ coating grow in intensity and shift towards the position of a stoichiometric h-AlN phase [46] during isothermal annealing at 1000 °C.

Fig. 6(a) shows the evolution of the cubic 200 interplanar spacing for both the dual-phase $Ti_{0.34}Al_{0.66}N_{0.96}$ and single-phase $Ti_{0.40}Al_{0.60}N_{0.94}$ coatings. In the single-phase coating, the cubic 200 diffraction peak displays slightly larger initial interplanar spacing than in the dual-phase coating. The overall lower Al-content in the single-phase coating contributes to this difference. The increase in interplanar spacing, observed up to 450 °C for both coatings, is assigned to thermal expansion. Between 450 °C and about 900 °C, a decrease of the interplanar spacing takes place in the single-phase coating, while it is approximately constant in the dual-phase coating. The decrease in interplanar spacing is associated with annihilation of point defects such as vacancies and interstitials [27]. It suggests that a larger amount of defect annihilation occurs in the single-phase compared to the dual-phase coatings. In CrN coatings it was observed that different activation energies for defect annihilation exist, which is correlated to the incident ion energy during growth [47]. Thus, the higher energy provided to the growth front in Mode I compared to Mode II (single-phase coating) [30] may result in different amounts and different types of point-defects in the two coatings. The increase of the interplanar spacing at temperatures above 900 °C and 850 °C for the single-phase and dual-phase coatings, respectively, is a result of Al-depletion of the cubic phase when h-AlN forms subsequent to spinodal decomposition. The interplanar spacing of the cubic phase reaches a stable value after about 30 and 90 min at 1000 °C for the dual- and single-phase coatings, respectively. The stable lattice parameter of both coatings is smaller than stoichiometric c-TiN at 1000 °C [48], indicated by the dashed line, suggesting that the cubic phase still contains Al. The lattice parameter for c-TiN at 1000 °C was calculated assuming a coefficient of thermal expansion of 9.35×10^{-6} °C^{-1} [49].

In Fig. 6(b), the evolution of the full width at half maximum (FWHM) of the cubic 200 diffraction peak is displayed for both samples. Initially, the dual-phase $Ti_{0.34}Al_{0.66}N_{0.96}$ coating shows greater FWHM than the single-phase $Ti_{0.40}Al_{0.60}N_{0.94}$ coating due to its smaller grain size. The decrease of FWHM observed in the dual-phase coating until about 750 °C is associated with an increase of grain size or reduction of microstrains. The increase of FWHM at about 800 °C is related to the formation of compositional modulations during spinodal decomposition. The maximum FWHM is

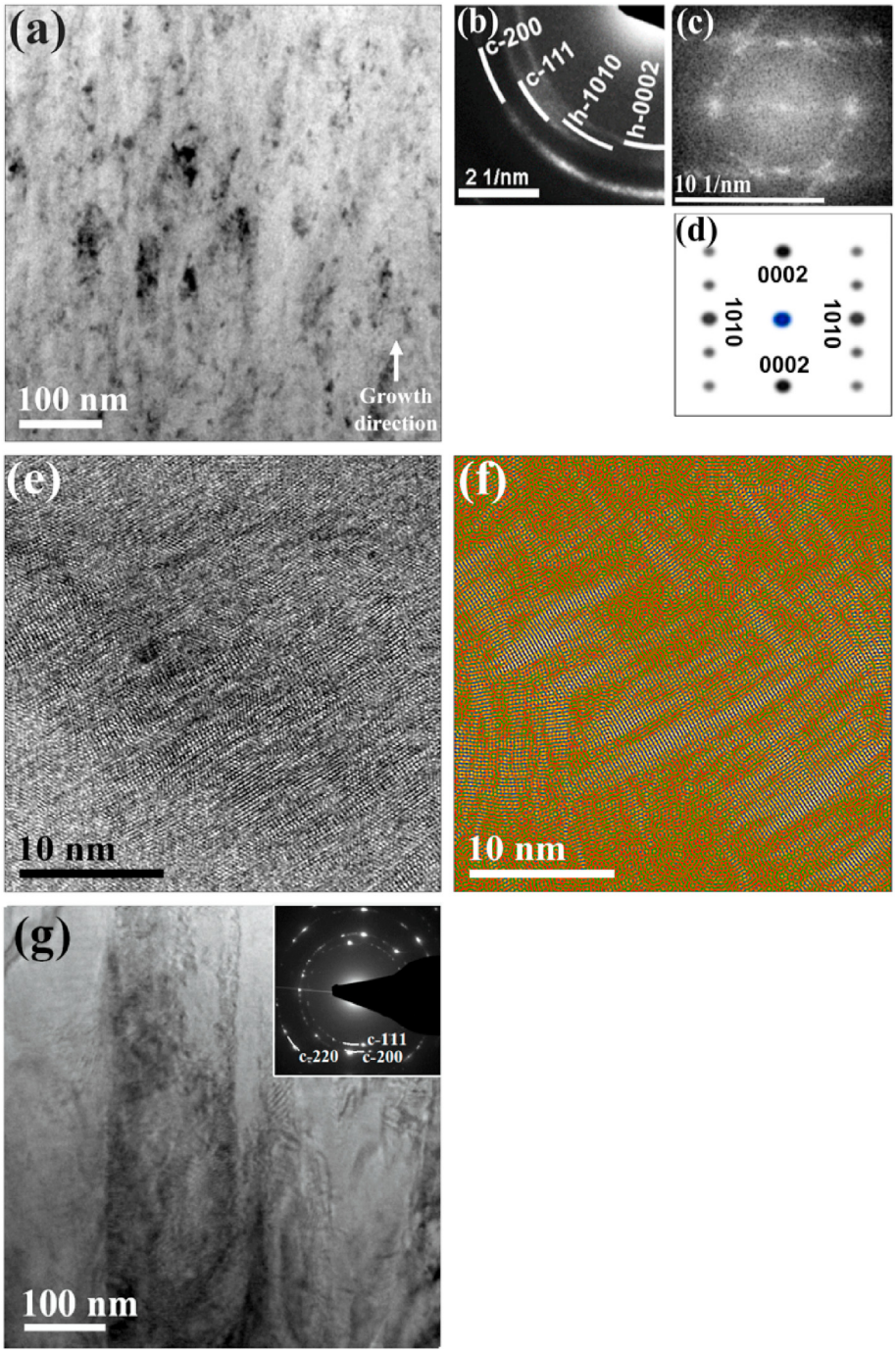

Fig. 3. TEM micrographs of the as-deposited coatings: (a–f) show the dual-phase $Ti_{0.34}Al_{0.66}N_{0.96}$ coating where (a) is a bright field overview, (b) is SAED of (a), (c) a FFT of (e), and (d) a simulation of the FFT pattern in (c). Figure (e) is a high resolution micrograph and (f) is an inverse FFT of (e) generated by selecting the spots from the hexagonal $10\bar{1}0$ and 0002 planes in the FFT in (c). Figure (g) is a bright field overview of the single-phase $Ti_{0.40}Al_{0.60}N_{0.94}$ coating and the insert is the corresponding SAED.

observed at a temperature 50 °C higher for the single-phase coating. This is likely an effect of the higher density of internal interphases, in the form of grain boundaries in the nanocrystalline dual-phase coating, directly affecting the spinodal decomposition by shifting it to lower temperatures [8].

Fig. 7 shows the evolution of the hexagonal $10\bar{1}0$ interplanar spacing and the FWHM of this diffraction peak for the two coatings. Until about 600 °C, an increase in the interplanar spacing is observed for dual-phase $Ti_{0.34}Al_{0.66}N_{0.96}$ coating as a result of thermal expansion. The change in thermal expansion seen for the cubic phase above 450 °C is not observed here, suggesting that either the defects in the hexagonal phase are relaxed at higher temperatures or that there are less defects in the hexagonal phase compared to the cubic phase. Between 600 °C and 800 °C, the interplanar spacing remains constant and it decreases above 800 °C. This deviation from a linear thermal expansion suggests that the interplanar spacing is affected by the phase transformations identified above.

In the dual-phase coating, cubic AlN-rich domains formed during spinodal decomposition subsequently transforms to a

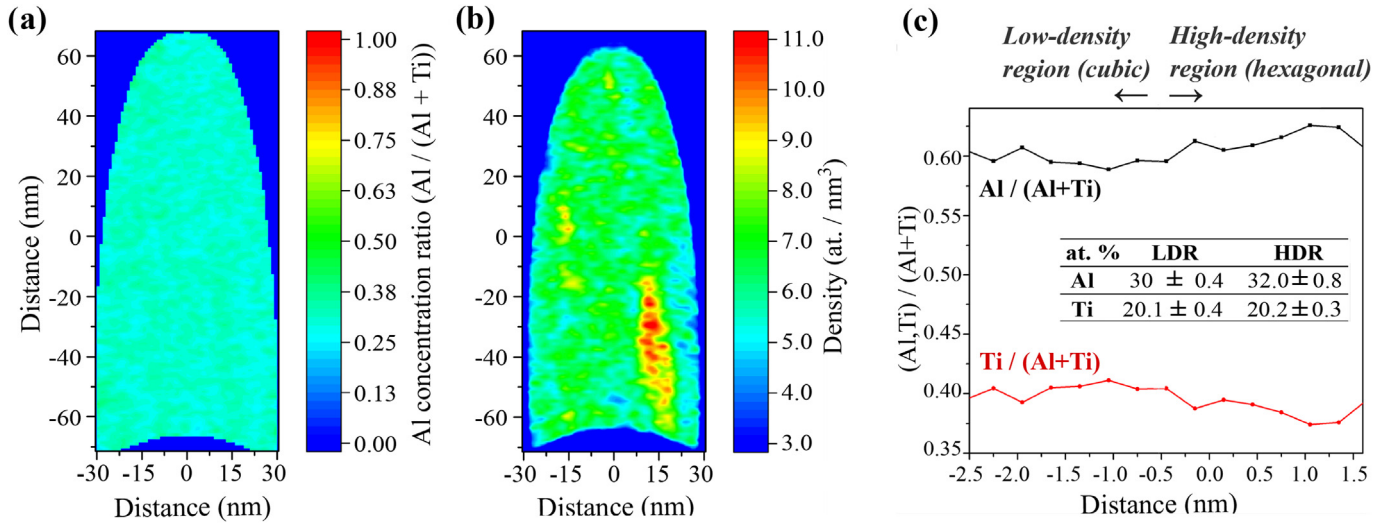

Fig. 4. Two-dimensional (2D) maps from a 3 nm slice across an APT reconstruction from the as-deposited dual-phase $Ti_{0.34}Al_{0.66}N_{0.96}$ coating. (a) shows an iso-concentration map of the Al distribution, and (b) an iso-density map. (c) is a proximity histogram displaying compositional variations inside and outside the higher-density region, interpreted as being the hexagonal phase. The histogram was constructed from an Al iso-density surface (Fig. 4(b)) with 8 atoms/nm^3.

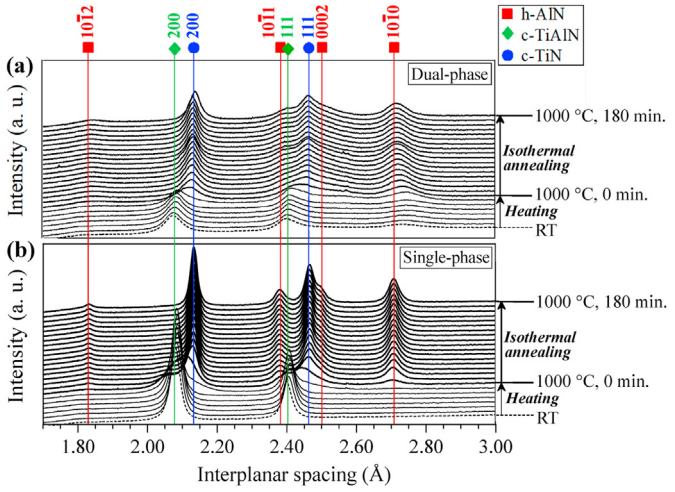

Fig. 5. WAXS lineouts from (a) dual-phase $Ti_{0.34}Al_{0.66}N_{0.96}$ and (b) single-phase $Ti_{0.40}Al_{0.60}N_{0.94}$ coatings showing phase evolution during the heating from room temperature (RT) to 1000 °C and the following isothermal annealing for 3 h. The dashed line at RT is data from the as-deposited coating, the thinner lines show data recorded during the heating from RT to 1000 °C, and the thicker lines show data from the isothermal annealing at 1000 °C.

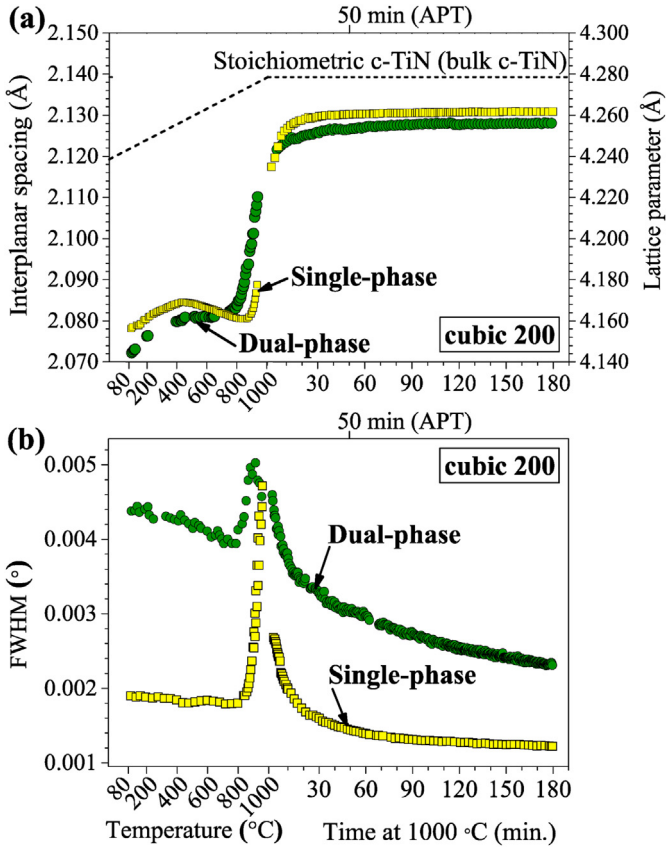

Fig. 6. Evolution of (a) interplanar spacing and (b) FWHM (peak broadening) of the cubic 200 diffraction peak during annealing.

hexagonal phase. The newly formed AlN-rich hexagonal-structured grains (here referred to as type II h-Al(Ti)N grains) co-exist with the AlN-rich hexagonal-structured grains formed during growth (referred to as type I h-Al(Ti)N grains). Thus, above 600 °C, the nucleation of type II h-Al(Ti)N grains with a higher Al-content compared to the type I h-Al(Ti)N grains combined with the purification (out-diffusion of Ti) of type I h-Al(Ti)N grains result in an overall decrease of the interplanar spacing. It is not possible, however, to separate the individual contributions of type I and type II h-Al(Ti)N grains on the interplanar spacing behavior. Grain growth is observed as a decreased FWHM above 600 °C (see Fig. 7(b)), and it occurs in both grain types.

In the single-phase $Ti_{0.40}Al_{0.60}N_{0.94}$ coating, the hexagonal phase was first detected at approximately 900 °C. After approximately 30 min of isothermal annealing at 1000 °C the interplanar spacing stabilizes at a value close to that of stoichiometric h-AlN [50], indicated by the dashed line in Fig. 7(a). The interplanar spacing of stoichiometric h-AlN at 1000 °C was calculated using a coefficient of thermal expansion of 4.2×10^{-6} °C^{-1} [51]. The h-AlN phase in the single-phase $Ti_{0.40}Al_{0.60}N_{0.94}$ coating originates from c-AlN domains formed during spinodal decomposition and displays an interplanar spacing slightly larger than stoichiometric h-AlN

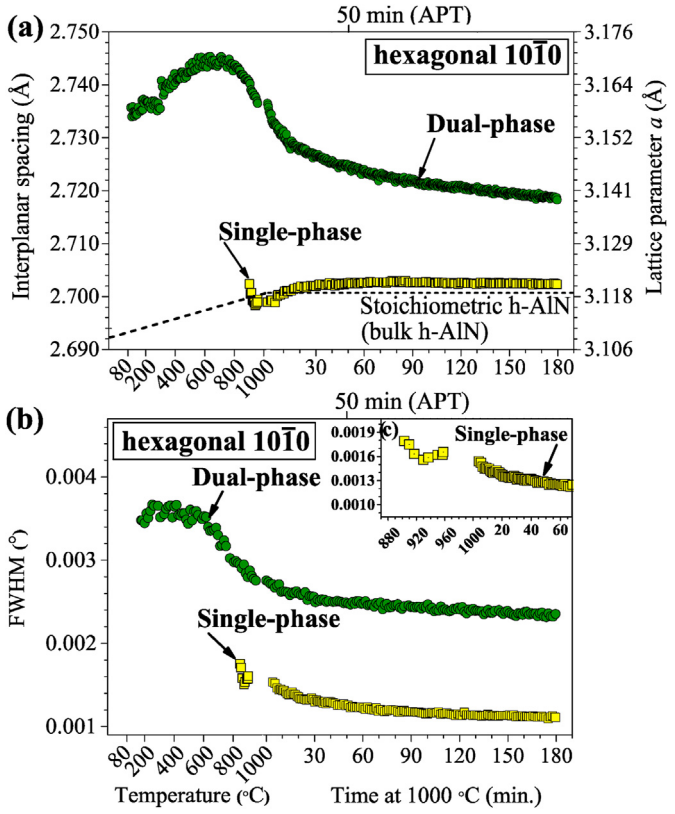

Fig. 7. Evolution of (a) interplanar spacing, and (b) FWHM of the hexagonal-10$\bar{1}$0 peak during annealing. (c) shows the detailed behavior of FWHM evolution for the single-phase sample.

even in early stages of h-AlN nucleation. This suggests the presence of small amounts of Ti-impurities in the h-AlN domains. However, the amount of Ti-impurities is larger in the dual-phase coating. For both coatings, grain growth of the h-AlN grains occurs when the temperature is increased, observed as a decreasing FWHM (Fig. 7(c)). The variations in FWHM below 1000 °C (Fig. 7(c)) are likely a result of the high nucleation rate at this stage, resulting in differences in the grain size distribution with temperature.

The nanostructures of the coatings change substantially during annealing while their macroscopic morphologies remain the same, as depicted in Fig. 3 (a) and (g). Fig. 8 shows 10 nm slices through APT reconstructions and composition for (a) the dual-phase $Ti_{0.34}Al_{0.66}N_{0.96}$ and (b) the single-phase $Ti_{0.40}Al_{0.60}N_{0.94}$ coatings, respectively, annealed at 1000 °C for 50 min. The dual-phase $Ti_{0.34}Al_{0.66}N_{0.96}$ coating (Fig. 8(a)) consists of nanometer sized domains of h-AlN that contains approximately 15 at.% Ti and c-TiN that contains approximately 5 at.% Al. The reconstructed single-phase coating (Fig. 8(b)), however, consists of hexagonal structured AlN-rich domains containing about 1.4 at.% of Ti and cubic structured TiN-rich domains containing about 2 at.% of Al.

Fig. 8(c) shows a proximity histogram for comparison of the concentration profiles of Al and Ti in AlN-rich (right) and TiN-rich (left) domains for both coatings. For the dual-phase $Ti_{0.34}Al_{0.66}N_{0.96}$ coating (solid lines), the Al- and Ti-content varies in both the AlN-rich and TiN-rich domains. For the AlN-rich domains assigned to the hexagonal phase, this can be understood as a mixture of type I and type II h-Al(Ti)N grains as discussed above. There is a relatively large change in Ti-content of the TiN-rich cubic phase, between the as-deposited and annealed state, i.e. from 20 at.% to 46 at.% (see Figs. 4 and 8). Meanwhile, the Ti-content in hexagonal-structured AlN-rich domains changes only from 20 at.% to 15 at.%. Furthermore, this is the average composition of close to stoichiometric type II and the type I h-Al(Ti)N grains. Thus, the change of Ti-content in type I h-Al(Ti)N grains is even smaller than 5 at.%. These compositional differences are probably caused by different diffusion scenarios. Diffusion is normally slower for atoms with larger atomic radius [52], thus the out-diffusion of Ti from type I h-Al(Ti)N can be expected to be slower compared to the out-diffusion of Al from the cubic phase formed during growth. This is further corroborated by the stronger directionality of the metal-N bonds in h-AlN compared to c-TiN that affects vacancies needed for diffusion, i.e., a higher energy is associated with vacancies in h-AlN than c-TiN [53].

The type II h-Al(Ti)N grains in both coatings are expected to be similar and to form with a very low Ti-content, as evident from the interplanar spacing that is close to that of stoichiometric h-AlN for the single phase coating (see Fig. 7(a)). Thus, the Al content of the type II h-Al(Ti)N grains in the dual-phase $Ti_{0.34}Al_{0.66}N_{0.96}$ coating is not expected to change substantially with time, and instead the observed small decrease rate of the interplanar spacing towards the Ti-free value during isothermal annealing (see Fig. 7(a)) is interpreted as slow out-diffusion of Ti from type I h-Al(Ti)N grains. Such out-diffusion in the type I h-Al(Ti)N grains is slower than in the cubic phase formed during growth. The single-phase coating (see Fig. 8(c) dashed lines) reveals AlN- and TiN-rich domains almost free from Ti and Al, respectively, with a constant Ti and Al concentration 3 nm away from the interphase.

Fig. 9 shows the evolution of strain extracted from the *in situ* WAXS data. In the as-deposited state, the single-phase $Ti_{0.40}Al_{0.60}N_{0.94}$ coating exhibits lower compressive strain (−0.8%) than the cubic phase of the dual-phase $Ti_{0.34}Al_{0.66}N_{0.96}$ coating (−1.3%) (Fig. 9(a)). The compressive strain of the cubic phase decreases in the single-phase coating up to about 900 °C. At 900 °C, the compressive strain starts to increase and oscillates at higher temperatures, until approximately 15 min of the isothermal annealing time has passed, associated with the formation of h-AlN. From this point, the compressive strain of the cubic phase continuously decreases until the end of the isothermal annealing. Similar variations in strain of the cubic phase during the initial formation of h-AlN and the subsequent formation of stoichiometric c-TiN has been previously reported [27]. **In Fig. 9(b)**, the strain in the hexagonal phase in the single-phase coating has a similar behavior as the cubic phase during isothermal annealing, with a slowly decreasing compressive strain. At the end of the isothermal annealing the cubic phase is close to strain free (Fig. 9(a)), while there is still a small compressive strain in the hexagonal phase (Fig. 9(a)). For the dual-phase $Ti_{0.34}Al_{0.66}N_{0.96}$ coating, the large width of the diffraction peaks of the cubic phase, especially during spinodal decomposition, restricts the strain data to be accurately determined during the first min of isothermal annealing at temperatures below 400 °C. However, the strain of the cubic phase is close to zero when the isothermal temperature is reached (Fig. 9(a)). The strain relaxation is considerably slower for the hexagonal phase where a significant level of compressive strain remains even after 3 h of isothermal annealing (Fig. 9(b)). The similar level of compressive strain in the cubic and hexagonal phases of the as-deposited dual-phase $Ti_{0.34}Al_{0.66}N_{0.96}$ coating suggests that the strain relaxation during annealing would the same for both phases. The retained compressive strain in the hexagonal phase is interpreted as a result of the presence of hexagonal grains with different chemical composition (type I and II h-Al(Ti)N).

Fig. 10 shows the as-deposited and post-annealed hardness values recorded at room temperature for the dual-phase $Ti_{0.34}Al_{0.66}N_{0.96}$ and single-phase $Ti_{0.40}Al_{0.60}N_{0.94}$ coatings. The single-phase coating exhibits higher as-deposited hardness (33.5 GPa) compared to the dual-phase coating, which is attributed

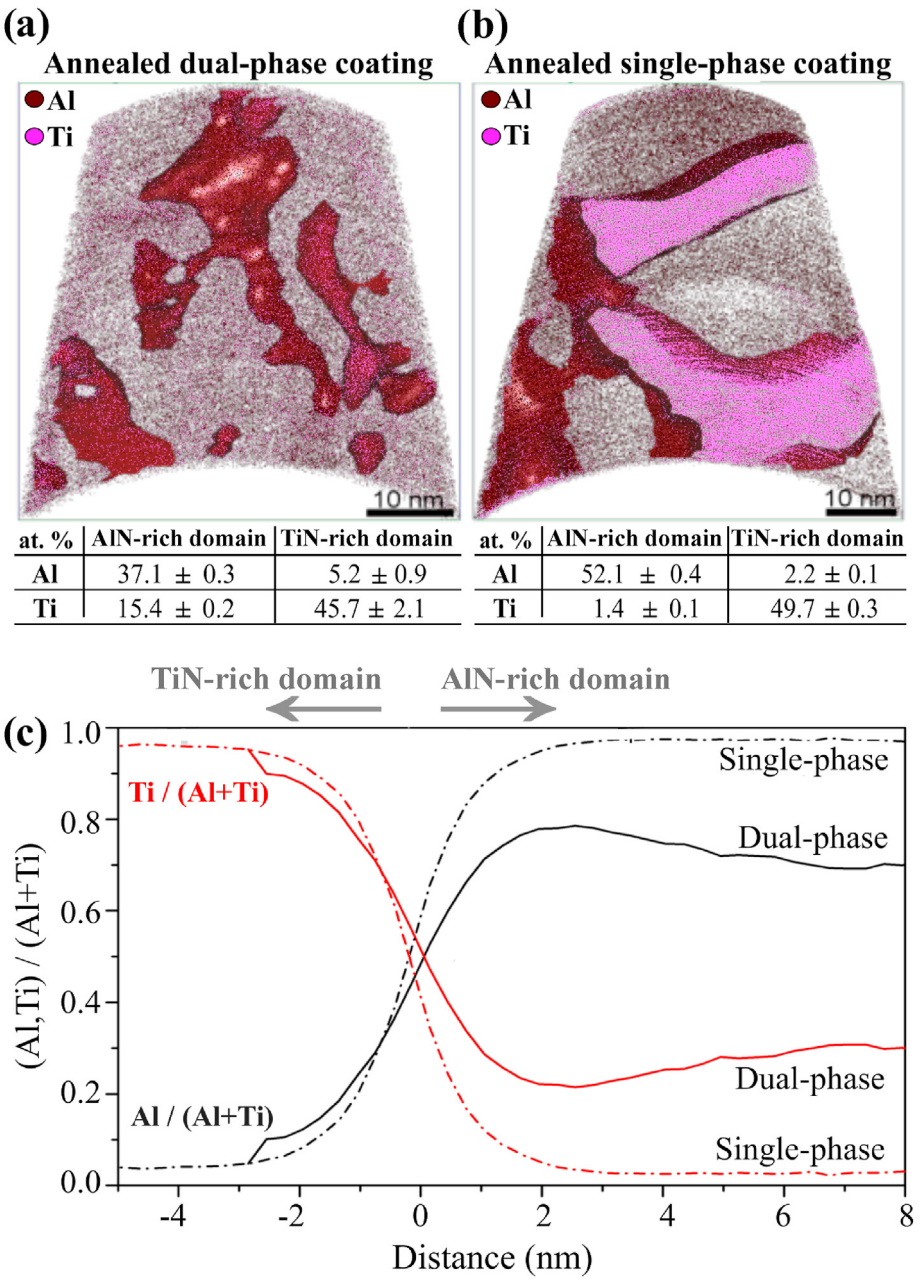

at. %	AlN-rich domain	TiN-rich domain
Al	37.1 ± 0.3	5.2 ± 0.9
Ti	15.4 ± 0.2	45.7 ± 2.1

at. %	AlN-rich domain	TiN-rich domain
Al	52.1 ± 0.4	2.2 ± 0.1
Ti	1.4 ± 0.1	49.7 ± 0.3

Fig. 8. Atomic maps of 10 nm slices through APT reconstructions and global composition tables after annealing for 50 min at 1000 °C: (a) Dual-phase $Ti_{0.34}Al_{0.66}N_{0.96}$ coating and (b) single-phase $Ti_{0.40}Al_{0.60}N_{0.94}$ coating. Domains are highlighted by an iso-concentration surface at 27 at.% Al; (c) Proximity histogram displaying composition profile of Ti and Al in TiN-rich and AlN-rich domains as a function of distance from the 27 at.% Al interface.

to the presence of type I h-Al(Ti)N [9,54] and a nanometer-sized grain structure [55–57]. Both coatings reveal a maximum hardness at the same annealing temperature which also corresponds to the temperature at which spinodal decomposition is initially observed (Fig. 5), i.e., at an annealing temperature of about 800 °C and 850 °C for the dual-phase coating and single-phase coating, respectively. The observed increase in hardness with annealing temperature has been attributed to the presence of coherency strains between cubic domains of different compositions [4]. For temperatures higher than 850 °C, both coatings show a decrease in hardness values, however, with a larger decay rate for the single-phase coating. The decrease in hardness has been correlated to the phase transformation from c-AlN to h-AlN [9,20], as well as grain growth, defect annihilation and strain relaxation (Fig. 9) [58]. Additionally, the dual-phase coating shows the lowest hardness at all annealing temperatures, likely a result of its nanocrystalline structure, in which grains typically smaller than 30 nm [59] contribute to plastic deformation by grain boundary sliding (inverse Hall-Petch relation) [60].

4. Conclusion

The different phase, microstructure, and strain evolutions of dual-phase $Ti_{0.34}Al_{0.66}N_{0.96}$ and single-phase $Ti_{0.40}Al_{0.60}N_{0.94}$ coatings were analyzed *in situ* during annealing at 1000 °C. For both coatings, spinodal decomposition of the cubic phase takes place during annealing. Decomposition starts at a lower temperature in the dual-phase coating due to the high density of grain boundaries.

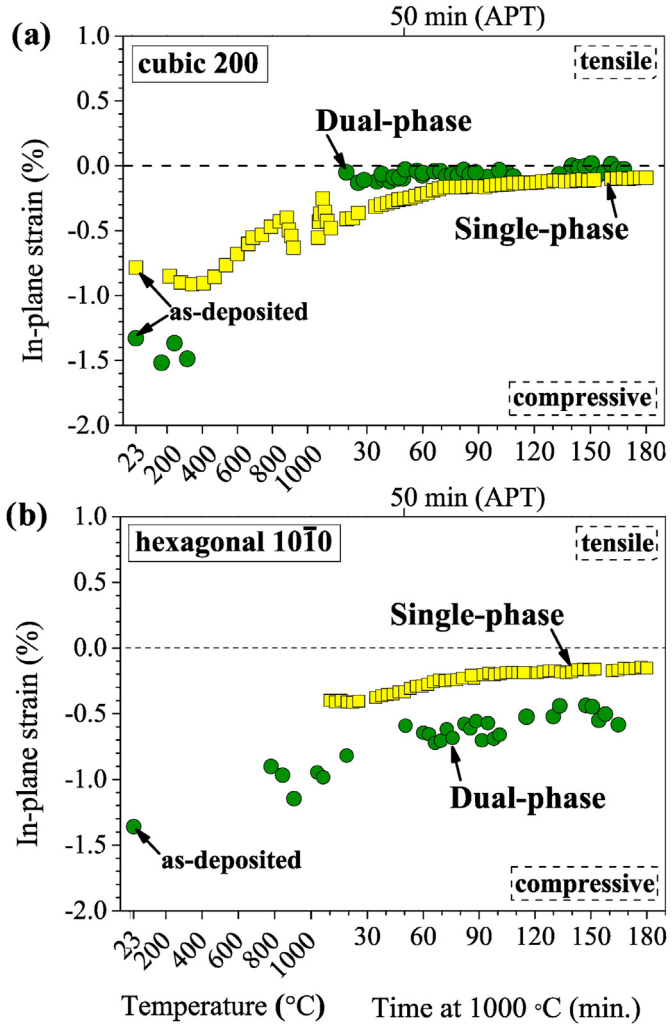

Fig. 9. Strain evolution during annealing: (a) in the cubic phase recorded using the 200 diffraction line and (b) in the hexagonal phase recorded using the 10$\bar{1}$0 diffraction line.

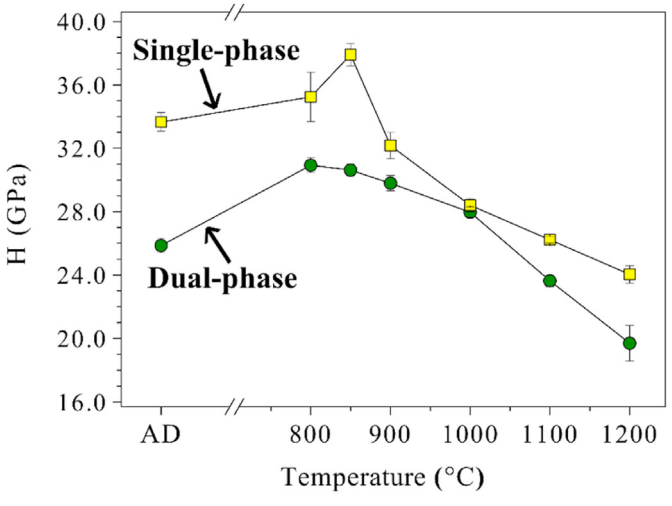

Fig. 10. Nanoindentation hardness of the coatings in the as-deposited state (AD) and post-annealed from 800 to 1200 °C for 50 min.

After 50 min of isothermal annealing, both coatings display a subsequent transformation of c-AlN domains to h-AlN. The hexagonal phase has a higher thermal stability than the cubic phase and, for the dual-phase coating, a substantial amount of Ti (>15 at.%) is still retained in this phase after 50 min of isothermal annealing. A larger amount of Al is retained in the cubic phase for the dual-phase coating (~5 at.%) compared to the single-phase coating (~2 at.%). For both coatings, the spinodal decomposition has a positive effect on the coating's hardness while the following formation of h-AlN causes the hardness to decrease. In summary, the thermal stability of TiAlN is strongly affected by its microstructure and should be considered when coatings are designed for high temperature applications. The microstructure offers a mean to tune the decomposition pathway favorably.

CRediT authorship contribution statement

A.B.B. Chaar: Conceptualization, Investigation, Writing - original draft. **L. Rogström:** Conceptualization, Investigation, Writing - review & editing, Supervision, Project administration. **M.P. Johansson-Jöesaar:** Conceptualization, Investigation, Resources, Writing - review & editing, Supervision. **J. Barrirero:** Investigation, Writing - review & editing. **H. Aboulfadl:** Investigation, Writing - review & editing. **N. Schell:** Resources. **D. Ostach:** Investigation. **F. Mücklich:** Resources, Supervision, Funding acquisition. **M. Odén:** Conceptualization, Resources, Writing - review & editing, Supervision, Project administration, Funding acquisition.

Declaration of competing interest

The authors declare that they have no known competing financial interests or personal relationships that could have appeared to influence the work reported in this paper.

Acknowledgements

The work was supported by the Swedish Research Council (grant no. 621-2012-4401), the Swedish government strategic research area grant (AFM - SFO MatLiU no. 2009—00971), the VINNOVA (FunMat-II project grant no. 2016—05156). The atom probe instrument was financed by the DFG and the Federal State Government of Saarland (INST 256/298-1 FUGG). The financial support of the Röntgen-Ångström Cluster (grant no. 2011—6505) enabled the access to PETRA III facilities. A. B. B. Chaar acknowledges the support from the European Union's Erasmus Mundus doctoral program in Materials Science and Engineering (DocMASE), and the Roberto Rocca Doctorate Fellowship. We thank Dr. Robert Boyd for the help with TEM operation and Dr. Mats Ahlgren, Dr. Lars Johnson, and Krister Edlund from Sandvik Coromant AB for their help with the coating depositions.

References

[1] V. Kumar, R. Penich, Stabilization of cubic phase in AlTiN coatings using anode configurations, Int. J. Refr. Metal. 60 (2016) 113—117.
[2] A. Knutsson, J. Ullbrand, L. Rogstrom, N. Norrby, J.S. Johnson, L. Hultman, J. Almer, M.P.J. Jõesaar, B. Jansson, M. Odén, Microstructure evolution during the isostructural decomposition of TiAlN-A combined in-situ small angle x-ray scattering and phase field study, J. Appl. Phys. 113 (2013) 213518.
[3] P.H. Mayrhofer, A. Hörling, L. Karlsson, J. Sjölen, T. Larsson, C. Mitterer, L. Hultman, Self-organized nanostructures in the Ti-Al-N system, Appl. Phys. Lett. 83 (10) (2003) 2049—2051.
[4] F. Tasnadi, I.A. Abrikosov, L. Rogström, J. Almer, M.P. Johansson, M. Odén, Significant elastic anisotropy in $Ti_{1-x}Al_xN$ alloys, Appl. Phys. Lett. 97 (2010) 231902.

[5] D. Rafaja, C. Wustefeld, M. Dopita, M. Motylenko, C. Baehtz, C. Michotte, M. Kathrein, Crystallography of phase transitions in metastable titanium aluminium nitride nanocomposites, Surf. Coating. Technol. 257 (2014) 26–37.
[6] N. Norrby, L. Rogström, M.P. Johansson-Jõesaar, N. Schell, M. Odén, In situ X-ray scattering study of the cubic to hexagonal transformation of AlN in $Ti_{(1-x)}Al_{(x)}N$, Acta Mater. 73 (2014) 205–214.
[7] A. Hörling, L. Hultman, M. Odén, J. Sjölen, L. Karlsson, Mechanical properties and machining performance of Ti1-xAlxN-coated cutting tools, Surf. Coating. Technol. 191 (2005) 384–392.
[8] A. Knutsson, I.C. Schramm, K.A. Grönhagen, F. Mucklich, M. Odén, Surface directed spinodal decomposition at TiAlN/TiN interfaces, J. Appl. Phys. 113 (2013) 114305.
[9] A. Hörling, L. Hultman, M. Odén, J. Sjölen, L. Karlsson, Thermal stability of arc evaporated high aluminum-content $Ti_{1-x}Al_xN$ thin films, J. Vac. Sci. Technol., A 20 (5) (2002) 1815–1823.
[10] B. Alling, A. Karimi, L. Hultman, I.A. Abrikosov, First-principles study of the effect of nitrogen vacancies on the decomposition pattern in cubic $Ti_{1-x}Al_xN_{1-y}$, Appl. Phys. Lett. 92 (2008) 71903.
[11] I.C. Schramm, M.P.J. Jöesaar, J. Jensen, F. Mucklich, M. Odén, Impact of nitrogen vacancies on the high temperature behavior of $(Ti_{1-x}Al_x)N_y$ alloys, Acta Mater. 119 (2016) 218–228.
[12] M. to Baben, M. Hans, D. Primetzhofer, S. Evertz, H. Ruess, J.M. Schneider, Unprecedented thermal stability of inherently metastable titanium aluminum nitride by point defect engineering, Mater. Res. Lett. 5 (2017) 158–169.
[13] N. Shulumba, O. Hellman, Z. Raza, B. Alling, J. Barrirero, F. Mucklich, I.A. Abrikosov, M. Odén, Lattice vibrations change the solid solubility of an alloy at high temperatures, Phys. Rev. Lett. 117 (2016) 205502.
[14] S. Liu, K. Chang, S. Mráz, X. Chen, M. Hans, D. Music, D. Primetzhofer, J.M. Schneider, Modeling of metastable phase formation for sputtered Ti1-xAlxN thin films, Acta Mater. 165 (2019) 615–625.
[15] N. Shulumba, Z. Raza, O. Hellman, E. Janzen, I.A. Abrikosov, M. Oden, Impact of anharmonic effects on the phase stability, thermal transport, and electronic properties of AlN, Phys. Rev. B 94 (2016) 104305.
[16] F. Pei, H.J. Liu, L. Chen, Y.X. Xu, Y. Du, Improved properties of TiAlN coating by combined Si-addition and multilayer architecture, J. Alloys Compd. 790 (2019) 909–916.
[17] H.K. Zou, L. Chen, K.K. Chang, F. Pei, Y. Du, Enhanced hardness and age-hardening of TiAlN coatings through Ru-addition, Scripta Mater. 162 (2019) 382–386.
[18] Y.H. Chen, J.J. Roa, C.H. Yu, M.P. Johansson-Joesaar, J.M. Andersson, M.J. Anglada, M. Oden, L. Rogstrom, Enhanced thermal stability and fracture toughness of TiAlN coatings by Cr, Nb and V-alloying, Surf. Coating. Technol. 342 (2018) 85–93.
[19] C.M. Koller, R. Hollerweger, C. Sabitzer, R. Rachbauer, S. Kolozsvari, J. Paulitsch, P.H. Mayrhofer, Thermal stability and oxidation resistance of arc evaporated TiAlN, TaAlN, TiAlTaN, and TiAlN/TaAlN coatings, Surf. Coating. Technol. 259 (2014) 599–607.
[20] A. Knutsson, M.P. Johansson, L. Karlsson, M. Odén, Thermally enhanced mechanical properties of arc evaporated $Ti_{(0.34)}Al_{(0.66)}N$/TiN multilayer coatings, J. Appl. Phys. 108 (2010), 044312.
[21] H. Lind, R. Forsen, B. Alling, N. Ghafoor, F. Tasnadi, M.P. Johansson, I.A. Abrikosov, M. Odén, Improving thermal stability of hard coating films via a concept of multicomponent alloying, Appl. Phys. Lett. 99 (9) (2011), 091903.
[22] G. Greczynski, J. Lu, J. Jensen, S. Bolz, W. Kölker, C. Schiffers, O. Lemmer, J.E. Greene, L. Hultman, A review of metal-ion-flux-controlled growth of metastable TiAlN by HIPIMS/DCMS co-sputtering, Surf. Coating. Technol. 257 (2014) 15–25.
[23] L. Zauner, P. Ertelthaler, T. Wojcik, H. Bolvardi, S. Kolozsvári, P.H. Mayrhofer, H. Riedl, Reactive HiPIMS deposition of Ti-Al-N: influence of the deposition parameters on the cubic to hexagonal phase transition, Surf. Coating. Technol. 382 (2020) 125007.
[24] J.M. Andersson, J. Vetter, J. Müller, J. Sjölén, Structural effects of energy input during growth of $Ti_{1-x}Al_xN$ ($0.55 \leq x \leq 0.66$) coatings by cathodic arc evaporation, Surf. Coating. Technol. 240 (2014) 211–220.
[25] M. Hans, D. Music, Y.-T. Chen, L. Patterer, A.O. Eriksson, D. Kurapov, J. Ramm, M. Arndt, H. Rudigier, J.M. Schneider, Crystallite size-dependent metastable phase formation of TiAlN coatings, Sci. Rep. 7 (1) (2017) 16096.
[26] R. Rachbauer, S. Massl, E. Stergar, D. Holec, D. Kiener, J. Keckes, J. Patscheider, M. Stiefel, H. Leitner, P.H. Mayrhofer, Decomposition pathways in age hardening of Ti-Al-N films, J. Appl. Phys. 110 (2) (2011), 023515.
[27] L. Rogström, J. Ullbrand, J. Almer, L. Hultman, B. Jansson, M. Odén, Strain evolution during spinodal decomposition of TiAlN thin films, Thin Solid Films 520 (17) (2012) 5542–5549.
[28] K.M. Calamba, J.F. Pierson, S. Bruyere, A.L. Febvrier, P. Eklund, J. Barrirero, F. Mucklich, R. Boyd, M.P.J. Jöesaar, M. Odén, Dislocation structure and microstrain evolution during spinodal decomposition of reactive magnetron sputtered heteroepixatial c-(Ti-0.37,Al-0.63)N/c-TiN films grown on MgO(001) and (111) substrates, J. Appl. Phys. 125 (10) (2019) 105301.
[29] D. Rafaja, C. Wustefeld, C. Baehtz, V. Klemm, M. Dopita, M. Motylenko, C. Michotte, M. Kathrein, Effect of internal interfaces on hardness and thermal stability of nanocrystalline $Ti_{0.5}Al_{0.5}N$ coatings, Metall. Mater. Trans. 42a (3) (2011) 559–569.
[30] A.B.B. Chaar, B. Syed, T.-W. Hsu, M. Johansson-Jöesaar, J.M. Andersson, G. Henrion, L.J.S. Johnson, F. Mücklich, M. Odén, The effect of cathodic arc guiding magnetic field on the growth of $(Ti_{0.36}Al_{0.64})N$ coatings, Coatings 9 (10) (2019) 660.
[31] Q. Luo, P.E. Hovsepian, Transmission electron microscopy and energy dispersive X-ray spectroscopy on the worn surface of nano-structured TiAlN/VN multilayer coating, Thin Solid Films 497 (1) (2006) 203–209.
[32] S.R.S.B.D. Cullity, Elements of X-Ray Diffraction, 2d ed., Prentice Hall, NJ, 2001.
[33] K. Thompson, D. Lawrence, D.J. Larson, J.D. Olson, T.F. Kelly, B. Gorman, In situ site-specific specimen preparation for atom probe tomography, Ultramicroscopy 107 (2–3) (2007) 131–139.
[34] B. Gault, Atom Probe Microscopy, Springer, New York, 2012.
[35] D.J. Larson, Local Electrode Atom Probe Tomography: A User's Guide, Springer, New York, 2013.
[36] O.C. Hellman, J.A. Vandenbroucke, J. Rüsing, D. Isheim, D.N. Seidman, Analysis of three-dimensional atom-probe data by the proximity histogram, Microsc. Microanal. 6 (2000) 437–444.
[37] W.C. Oliver, G.M. Pharr, An improved technique for determining hardness and elastic-modulus using load and displacement sensing indentation experiments, J. Mater. Res. 7 (6) (1992) 1564–1583.
[38] A.O. Eriksson, J.Q. Zhu, N. Ghafoor, M.P. Johansson, J. Sjölen, J. Jensen, M. Odén, L. Hultman, J. Rosén, Layer formation by resputtering in Ti–Si–C hard coatings during large scale cathodic arc deposition, Surf. Coating. Technol. 205 (15) (2011) 3923–3930.
[39] I.C. Schramm, C. Pauly, M.P. Johansson Jõesaar, S. Slawik, S. Suarez, F. Mücklich, M. Odén, Effects of nitrogen vacancies on phase stability and mechanical properties of arc deposited $(Ti_{0.52}Al_{0.48})Ny$ (y<1) coatings, Surf. Coating. Technol. 330 (2017) 77–86.
[40] I. Povstugar, P.-P. Choi, D. Tytko, J.-P. Ahn, D. Raabe, Interface-directed spinodal decomposition in TiAlN/CrN multilayer hard coatings studied by atom probe tomography, Acta Mater. 61 (20) (2013) 7534–7542.
[41] I. El Azhari, J. Barrirero, J. García, F. Soldera, L. Llanes, F. Mücklich, Atom Probe Tomography investigations on grain boundary segregation in polycrystalline Ti(C,N) and Zr(C,N) CVD coatings, Scripta Mater. 162 (2019) 335–340.
[42] D.J. Larson, B. Gault, B.P. Geiser, F. De Geuser, F. Vurpillot, Atom probe tomography spatial reconstruction: status and directions, Curr. Opin. Solid St. M. 17 (5) (2013) 236–247.
[43] U. Wahlström, L. Hultman, J.E. Sundgren, F. Adibi, I. Petrov, J.E. Greene, Crystal growth and microstructure of polycrystalline $Ti_{1-x}Al_xN$ alloy films deposited by ultra-high-vacuum dual-target magnetron sputtering, Thin Solid Films 235 (1) (1993) 62–70.
[44] R. Forsén, M.P. Johansson, M. Odén, N. Ghafoor, Effects of Ti alloying of AlCrN coatings on thermal stability and oxidation resistance, Thin Solid Films 534 (2013) 394–402.
[45] K.M. Calamba, J. Barrirero, M.P.J. Jõesaar, S. Bruyère, R. Boyd, J.F. Pierson, A. Le Febvrier, F. Mücklich, M. Odén, Growth and high temperature decomposition of epitaxial metastable wurtzite $(Ti_{1-x},Al_x)N(0001)$ thin films, Thin Solid Films 688 (2019) 137414.
[46] I.C.f.D. Data, AlN, PDF File No. 03-065-0831, 1998.
[47] J. Almer, M. Odén, L. Hultman, G. Håkansson, Microstructural evolution during tempering of arc-evaporated Cr–N coatings, J. Vac. Sci. Technol., A 18 (1) (2000) 121–130.
[48] V. Valvoda, Structure of thin-films of titanium nitride, J. Alloys Compd. 219 (1995) 83–87.
[49] H.O. Pierson, Handbook of Refractory Carbides and Nitrides : Properties, Characteristics, Processing, and Applications, Noyes Publications, Park Ridge, N.J., 1996.
[50] D. Nilsson, E. Janzen, A. Kakanakova-Georgieva, Lattice parameters of AlN bulk, homoepitaxial and heteroepitaxial material, J. Phys. D 49 (2016) 175108.
[51] G.A. Slack, S.F. Bartram, Thermal-expansion of some diamond-like crystals, J. Appl. Phys. 46 (1) (1975) 89–98.
[52] W.D. Callister, Materials Science and Engineering : an Introduction, fifth ed., Wiley, New York, 2000.
[53] F. Tasnádi, A.V. Lugovskoy, M. Odén, I.A. Abrikosov, Non-equilibrium vacancy formation energies in metastable alloys - a case study of $Ti_{0.5}Al_{0.5}N$, Mater. Des. 114 (2017) 484–493.
[54] M.P.J. Joesaar, N. Norrby, J. Ullbrand, R. M'Saoubi, M. Oden, Anisotropy effects on microstructure and properties in decomposed arc evaporated $Ti_{1-x}Al_xN$ coatings during metal cutting, Surf. Coating. Technol. 235 (2013) 181–185.
[55] C.E. Carlton, P.J. Ferreira, What is behind the inverse Hall-Petch effect in nanocrystalline materials? Acta Mater. 55 (11) (2007) 3749–3756.
[56] S.S. Quek, Z.H. Chooi, Z.X. Wu, Y.W. Zhang, D.J. Srolovitz, The inverse hall-petch relation in nanocrystalline metals: a discrete dislocation dynamics analysis, J. Mech. Phys. Solid. 88 (2016) 252–266.
[57] V. Yamakov, D. Wolf, S.R. Phillpot, A.K. Mukherjee, H. Gleiter, Deformation mechanism crossover and mechanical behaviour in nanocrystalline materials, Phil. Mag. Lett. 83 (6) (2003) 385–393.
[58] L. Karlsson, A. Hörling, M.P. Johansson, L. Hultman, G. Ramanath, The influence of thermal annealing on residual stresses and mechanical properties of arc-evaporated TiC_xN_{1-x} (x=0, 0. 15 and 0.45) thin films, Acta Mater. 50 (20) (2002) 5103–5114.
[59] S.N. Naik, S.M. Walley, The Hall–Petch and inverse Hall–Petch relations and the hardness of nanocrystalline metals, J. Mater. Sci. 55 (7) (2020) 2661–2681.
[60] H. Hahn, K.A. Padmanabhan, A model for the deformation of nanocrystalline materials, Philos. Mag. A B 76 (4) (1997) 559–571.